Parabolic BM-scan technique for full range doppler spectral domain optical coherence tomography

Franck Jaillon[*], Shuichi Makita, Masaki Yabusaki, and Yoshiaki Yasuno[**]

Computational Optics Group in the University of Tsukuba,
1-1-1 Tennodai, Tsukuba, Ibaraki 305-8573, Japan
[*]*franck.jaillon@optlab2.bk.tsukuba.ac.jp*

Abstract: A full range spectral domain optical coherence tomography (SD-OCT) technique that relies on the linear phase modulation of one of the interferometer arms has been widely utilized. Although this method is useful, the mirror image elimination is not perfect for samples in which regions with high axial motion exist. In this paper, we introduce a new modulation pattern to overcome this mirror image elimination failure. This new modulation is a parabolic phase modulation in the transverse scanning direction, and is applied to the SD-OCT reference beam by an electro-optic modulator. Flow phantom and *in vivo* experiments demonstrate that for moving structures with large velocities, this parabolic phase modulation technique presents better mirror image elimination than a standard linear phase modulation method. A direct consequence of this enhanced mirror image removal is an improved velocity range obtained with phase-resolved Doppler imaging. Consequently, applying the proposed technique in retinal blood flow measurements may be useful for ophthalmologic diagnosis.

OCIS codes: (170.4500) Optical coherence tomography; (170.4470) Ophthalmology; (170.3880) Medical and biological imaging

References and links

1. D. Huang, E. A. Swanson, C. P. Lin, J. S. Schuman, W. G. Stinson, W. Chang, M. R. Hee, T. Flotte, K. Gregory, C. A. Puliafito, and J. G. Fujimoto, "Optical coherence tomography," Science **254**, 117881, (1991).
2. A. F. Fercher, C. K. Hitzenberger, G. Kamp, and S. Y. El-Zaiat, "Measurement of intraocular distances by backscattering spectral interferometry," Opt. Commun. **117**, 43–8, (1995).
3. R. Leitgeb, C. K. Hitzenberger, and A. F. Fercher, "Performance of Fourier domain vs. time domain optical coherence tomography," Opt. Express **11**(8), 889–894 (2003), http://www.opticsinfobase.org/oe/abstract.cfm?uri=oe-11-8-889.
4. R. Leitgeb, L. Schmetterer, C. K. Hitzenberger, A. F. Fercher, F. Berisha, M. Wojtkowski, and T. Bajraszewski, "Real-time measurement of in vitro flow by Fourier-domain color Doppler optical coherence tomography," Opt. Lett. **29**(2), 171–173 (2004), http://www.opticsinfobase.org/ol/abstract.cfm?URI=ol-29-2-171.
5. B. Vakoc, S. Yun, J. de Boer, G. Tearney, and B. Bouma**, "**Phase-resolved optical frequency domain imaging**,"** Opt. Express **13**(14), 5483–5493 (2005), http://www.opticsinfobase.org/abstract.cfm?URI=oe-13-14-5483
6. R. M. Werkmeister, N. Dragostinoff, M. Pircher, E. Götzinger, C. K. Hitzenberger, R. A. Leitgeb, and L. Schmetterer , "Bidirectional Doppler Fourier-domain optical coherence tomography for measurement of absolute flow velocities in human retinal vessels," Opt. Lett. **33**(24), 2967–2969 (2008), http://www.opticsinfobase.org/abstract.cfm?URI=ol-33-24-2967 .
7. Y. Yasuno, S. Makita, Y. Sutoh, M. Itoh, and T. Yatagai, "Birefringence imaging of human skin by polarization-sensitive spectral interferometric optical coherence tomography," Opt. Lett. **27**(20), 1803–1805 (2002), http://www.opticsinfobase.org/ol/abstract.cfm?URI=ol-27-20-1803.

#121349 - $15.00 USD Received 11 Dec 2009; revised 7 Jan 2010; accepted 7 Jan 2010; published 12 Jan 2010

8. E. Götzinger, M. Pircher, and C. K. Hitzenberger, "High speed spectral domain polarization sensitive optical coherence tomography of the human retina," Opt. Express **13**(25), 10217–10229 (2005), http://www.opticsinfobase.org/oe/abstract.cfm?URI=oe-13-25-10217.
9. M. Pircher, E. Gotzinger, R. Leitgeb, H. Sattmann, O. Findl, and C. K. Hitzenberger, "Imaging of polarization properties of human retina in vivo with phase resolved transversal PS-OCT," Opt. Express **12**(24), 5940–5951 (2004), http://www.opticsexpress.org/abstract.cfm?URI=OPEX-12-24-5940.
10. M. Yamanari, S. Makita, D.V. Madjarova, T. Yatagai, and Y. Yasuno, "Fiber-Based Polarization-Sensitive Fourier Domain Optical Coherence Tomography using B-Scan-Oriented Polarization Modulation Method," Opt. Express **14**(14), 6502–6515 (2006), http://www.opticsinfobase.org/abstract.cfm?URI=oe-14-14-6502.
11. C. Lu, C. Lee, M. Tsai, Y. Wang, and C. C. Yang, "Measurement of the hemoglobin oxygen saturation level with spectroscopic spectral-domain optical coherence tomography," Opt. Lett. **33**(5), 416–418 (2008), http://www.opticsinfobase.org/abstract.cfm?URI=ol-33-5-416.
12. A. Bachmann, R. Leitgeb, and T. Lasser, "Heterodyne Fourier domain optical coherence tomography for full range probing with high axial resolution," Opt. Express **14**(4), 1487–1496 (2006), http://www.opticsinfobase.org/oe/abstract.cfm?uri=oe-14-4-1487.
13. B. Vakoc, S. Yun, G. Tearney, and B. Bouma, "Elimination of depth degeneracy in optical frequency-domain imaging through polarization-based optical demodulation," Opt. Lett. **31**(3), 362–364 (2006), http://www.opticsinfobase.org/ol/abstract.cfm?URI=ol-31-3-362.
14. M. A. Choma, C. Yang, and J. A. Izatt, "Instantaneous quadrature low-coherence interferometry with 3×3 fiber optic couplers," Opt. Lett. **28**(22), 2162–2164 (2003), http://www.opticsinfobase.org/ol/abstract.cfm?URI=ol-28-22-2162.
15. M. V. Sarunic, B. E. Applegate, and J. A. Izatt, "Real-time quadrature projection complex conjugate resolved Fourier domain optical coherence tomography," Opt. Lett. **31**(16), 2426–2428 (2006), http://www.opticsinfobase.org/ol/abstract.cfm?URI=ol-31-16-2426.
16. A. Vakhtin, K. Peterson, and D. Kane, "Resolving the complex conjugate ambiguity in Fourier-domain OCT by harmonic lock-in detection of the spectral interferogram," Opt. Lett. **31**(9), 1271–1273 (2006), http://www.opticsinfobase.org/ol/abstract.cfm?URI=ol-31-9-1271.
17. M. Wojtkowski, A. Kowalczyk, R. Leitgeb, and A. Fercher, "Full range complex spectral optical coherence tomography technique in eye imaging," Opt. Lett. **27**(16), 1415–1417 (2002), http://www.opticsinfobase.org/ol/abstract.cfm?URI=ol-27-16-1415.
18. R. A. Leitgeb, C. K. Hitzenberger, A. F. Fercher, and T. Bajraszewski, "Phase-shifting algorithm to achieve high speed long-depth-range probing by frequency-domain optical coherence tomography," Opt. Lett. **28**(22), 2201–2203 (2003), http://www.opticsinfobase.org/ol/abstract.cfm?uri=ol-28-22-2201.
19. Y. K. Tao, M. Zhao, and J. A. Izatt, "High-speed complex conjugate resolved retinal spectral domain optical coherence tomography using sinusoidal phase modulation," Opt. Lett. **32**(20), 2918–2920 (2007), http://www.opticsinfobase.org/ol/abstract.cfm?URI=ol-32-20-2918.
20. R. K. Wang, "In vivo full range complex Fourier domain optical coherence tomography," Appl. Phys. Lett. **90**(5), 054103 (2007).
21. E. Götzinger, M. Pircher, R. A. Leitgeb, and C. K. Hitzenberger, "High speed full range complex spectral domain optical coherence tomography," Opt. Express **13**(2), 583–594 (2005), http://www.opticsinfobase.org/oe/abstract.cfm?uri=oe-13-2-583.
22. Y. Yasuno, S. Makita, T. Endo, G. Aoki, M. Itoh, and T. Yatagai, "Simultaneous *B*–*M*-mode scanning method for real-time full-range Fourier domain optical coherence tomography," Appl. Opt. **45**(8), 1861–1865 (2006), http://www.opticsinfobase.org/ao/abstract.cfm?URI=ao-45-8-1861.
23. M. Szkulmowski, A. Szkulmowska, T. Bajraszewski, A. Kowalczyk, and M. Wojtkowski, "Flow velocity estimation using joint Spectral and Time domain Optical Coherence Tomography," Opt. Express **16**(9), 6008–6025 (2008), http://www.opticsinfobase.org/oe/abstract.cfm?uri=oe-16-9-6008.
24. M. Szkulmowski, I. Grulkowski, D. Szlag, A. Szkulmowska, A. Kowalczyk, and M. Wojtkowski, "Flow velocity estimation by complex ambiguity free joint Spectral and Time domain Optical Coherence Tomography," Opt. Express **17**(16), 14281–14297 (2009), http://www.opticsinfobase.org/oe/abstract.cfm?uri=oe-17-16-14281.
25. B. Baumann, M. Pircher, E. Götzinger, and C. K. Hitzenberger, "Full range complex spectral domain optical coherence tomography without additional phase shifters," Opt. Express **15**(20), 13375–13387 (2007), http://www.opticsinfobase.org/oe/abstract.cfm?uri=oe-15-20-13375.
26. R. A. Leitgeb, R, Michaely, T, Lasser, and S. Chandra Sekhar, "Complex ambiguity-free Fourier domain optical coherence tomography through transverse scanning," Opt. Lett. **32**(23), 3453–3455 (2007), http://www.opticsinfobase.org/ol/abstract.cfm?URI=ol-32-23-3453.
27. S. Makita, T. Fabritius and Y. Yasuno, "Full-range, high-speed, high-resolution 1-μm spectral-domain optical coherence tomography using BM-scan for volumetric imaging of the human posterior eye," Opt. Express **16**(12), 8406–8420, (2008), http://www.opticsinfobase.org/oe/abstract.cfm?uri=oe-16-12-8406.

#121349 - $15.00 USD Received 11 Dec 2009; revised 7 Jan 2010; accepted 7 Jan 2010; published 12 Jan 2010

28. Y. K. Tao, K. M. Kennedy, and J. A. Izatt, "Velocity-resolved 3D retinal microvessel imaging using single-pass flow imaging spectral domain optical coherence tomography," Opt. Express **17** (5), 4177–4188 (2009), http://www.opticsinfobase.org/oe/abstract.cfm?uri=oe-17-5-4177.
29. *American National Standard Institute for the Safe Use of Lasers ANSI Z136.1-2000* (American National Standards institute, New York, 2000).

1. Introduction

Optical Coherence Tomography (OCT) is a three-dimensional non-invasive and non-contact imaging technique capable of producing structural micrometer scale cross-sectional images of scattering media, such as biological tissues. Time domain OCT (TD-OCT) was first described in the early 1990s [1]. Spectral domain optical coherence tomography (SD-OCT) [2] was later reported and has become a powerful alternative to TD-OCT because of its high sensitivity [3] and fast image acquisition. SD-OCT has also been extended to measure the blood flow [4, 5, 6], polarization properties [7–10], and spectroscopic properties of tissues [11]. However, SD-OCT has an intrinsic problem, the existence of complex ambiguity, the so-called mirror image artifact. This mirror image artifact occupies half the depth measurement range; thus, reducing the measurable depth of SD-OCT. Hence, suppressing this artifact results in doubling the depth range, and enables the use of the imaging region close to the zero delay line. Since the region close to the zero-delay line is known to have the highest sensitivity, this suppression of the mirror artifact provides the two benefits of a wide depth range and high sensitivity.

Different methods have been reported to remove the mirror image. These are based on phase-shifting interferometry. They can be classified into two main categories: (i) static [12–16] and (ii) sequential [17–27] acquisitions of A-lines with different shifted phases. Among the methods in the second category, the BM–scan method [22] is less sensitive to sample motions. In this paper, we refer to the method of acquiring a full range image by linearly phase-shifting the OCT signal in the B-scan direction as a standard or linear BM-scan. This method has the advantage of removing the complex ambiguity without sacrificing the measurement time. Although the BM-scan method has been successfully applied to in vivo applications [27], it has been found that the elimination of the mirror image with this method is not perfect if the sample has high velocity. For example, for large retinal blood vessels, the OCT signal is degraded and its mirror image appears.

In this paper, we present a new BM-scan method that uses parabolic phase modulation in the transverse scan direction to overcome this problem. The theory and experiments show that this parabolic BM-scan method is robust for the measurement of a sample with a high axial velocity. In vivo robust full depth-range imaging and associated Doppler OCT measurements with a wide velocity range are presented.

2. Theory

2.1. Standard BM-scan method

In order to understand the limitations of the standard (or linear) BM-scan method, we first explain the effects of sample axial motions on the efficiency of mirror image elimination.

In SD-OCT, the acquired spectral interferometric signal can be written as a function of the wavenumber k and time t as:

#121349 - $15.00 USD Received 11 Dec 2009; revised 7 Jan 2010; accepted 7 Jan 2010; published 12 Jan 2010

$$I(k,t) = I_0(k)\ \{\ \sum_m R_m + R_R + 2\sum_m \sqrt{R_R R_m}\cos\left[2k(z_R - z_m(t))\right] + \sum_m \sum_n \sqrt{R_m R_n}\cos\left[2k(z_n(t) - z_m(t))\right]\ \} \quad (1)$$

where $I_0(k)$ is the spectral density of the light source; R_R, R_n, and R_m are the reflectivities of the reference mirror, and the *n*-th and *m*-th interfaces of the sample, respectively. z_R, $z_n(t)$, and $z_m(t)$ are the axial positions of the reference mirror, and the *n*-th and *m*-th inner interfaces of the sample, respectively. The first and second terms on the right hand side of Eq. (1) represent the DC components of the OCT signal. These terms are not affected by the sample motion and are going to be eliminated by the BM-scan method. The fourth term is the autocorrelation term. This term may be affected by the sample motion. However, the amplitude of this term is sufficiently lower than other terms and can be neglected. The 3rd term is the combination of the OCT signal and its mirror signal. We thus focus our attention on the 3rd term on the right hand side.

We assume that the axial motion of the *m*-th interface is expressed as:

$$z_m(t) = z_0 + v_z t + a_z t^2 \quad (2)$$

where z_0 is the initial position of $z_m(t)$, v_z is the velocity, and a_z is the acceleration. By positioning a phase modulation device, such as an electro-optic modulator (EOM) or a piezoelectric transducer (PZT) mounted mirror, in the reference arm, a phase modulation is added during the transverse scanning (B-scan). In the case of linear phase modulation (standard BM-scan method), the additional phase term, φ', generated by the phase modulation device, is $\varphi' = \varepsilon' t$, where $\varepsilon' = \pi/(2\tau_A)$, with τ_A being the acquisition time for one A-line. Thus, after substitution of $z_m(t)$ by Eq. (2), addition of φ' and factorization, the total phase of the 3rd term of Eq. (1) becomes:

$$\varphi(t) = 2k\left((z_0 - z_R) + \left(v_z + \frac{\varepsilon'}{2k}\right)t + a_z t^2\right). \quad (3)$$

In the standard BM-scan method (see Fig. 1), a discrete Fourier transform is performed along the time axis *t* (Fig. 1(A)), namely in the transverse direction, and the signal is transformed into spatial frequency domain *f*. If we neglect the second order term in Eq. (3), this results in a shift in the spatial frequency domain, *f*, which is equal to:

$$2kv_z + \varepsilon', \quad (4)$$

depending on the EOM modulation ε' and on the axial velocity, v_z. Note that $\varepsilon' = \pi/2\tau_A$ makes it possible to offset the signal to the center of the positive *f* space. Therefore, if the sample or its inner structures are moving then additional shifts will be seen with respect to the EOM offset, leading to a broadening of the spectrum (Fig. 1(B)). The mirror image undergoes the opposite shift in the negative part of the *f* space and is filtered out with a numerical band-pass filter (red curve in Fig. 1(B)) [27]. The inverse Fourier transform of these filtered spectra is carried out along *f*. Finally, the Fourier transform is applied along *k* to generate the full range OCT image (Fig. 1(C)).

#121349 - $15.00 USD Received 11 Dec 2009; revised 7 Jan 2010; accepted 7 Jan 2010; published 12 Jan 2010

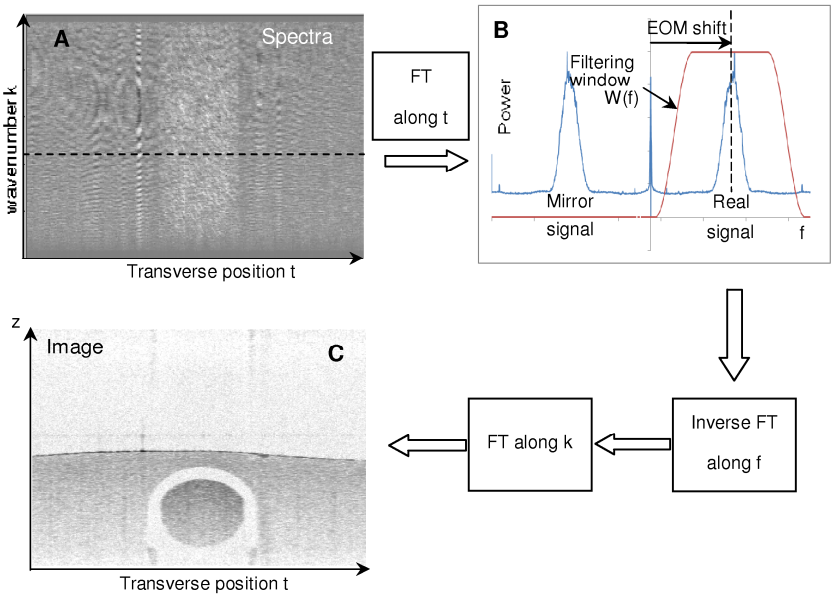

Fig. 1. Diagram of the standard BM-scan method: (A) starting from the real spectra (wavenumber *k*, transverse position *t* = time), a Fourier transform (FT) along the *t* direction is carried out to (B) filter the shifted (by EOM) mirror signal (*f* is the reciprocal space of the transverse dimension *t*). Inverse Fourier transforms along *f* and FT along *k* give (C) the final mirror free image (Depth *z*, transverse position *t*).

2.2. Limitation of standard BM-scan technique

A drawback of the standard BM-scan method is found in Eq. (4) and can be seen in Fig. 1(B). If the signal shift (from the EOM offset) due to v_z in the spatial frequency domain is larger than half the bandwidth of the numerical band pass filter applied to clip out the mirror image, the true OCT signal is undesirably filtered out. Note again that for optimum mirror image removal, ε' is chosen so that the phase shift in the spatial frequency domain, *f*, induced by the EOM is centered in the positive part of the *f* domain of the discrete Fourier transform. This condition is described as $\varepsilon' = \pi/(2\tau_A)$, where τ_A is the time interval between adjacent A-lines, determined by the CCD acquisition rate of the SD-OCT spectrometer. If the bandwidth of the band-pass filter is chosen to be equal to the width of the positive space *f* (equivalent to π/τ_A), then velocities larger than $v_z^{\max}$ such as $2kv_z^{\max}\tau_A = \pi/2$ or $v_z^{\max} = \lambda/(8\tau_A)$ (λ is the source wavelength in the medium) will be filtered out and the corresponding OCT signal in the reconstructed image will be missing. In our system (see Section 3), for example, λ_0 = 1020 nm and $1/\tau_A$ = 46.9 kHz, and the axial velocity limit is then approximately 4.4 mm/s (assuming a medium refractive index = 1.35). Therefore, in the case of *in vivo* applications such as retinal blood flow measurements [28], or where axial eye motions exist, this axial velocity limit may be reached, which may corrupt the OCT signal.

2.3. Parabolic BM-scan technique

We introduce a new modulation pattern, specifically parabolic phase modulation, to overcome the abovementioned limitation of the standard BM-scan method. Therefore, in the proposed method, the phase modulation applied to the EOM in the B-scan direction becomes $\varphi'' = \varepsilon'' t^2$, with $\varepsilon'' = \pi/(4\tau_A^2)$ and τ_A as the CCD acquisition time. Thus, the phase term of Eq. (3) now becomes:

#121349 - $15.00 USD Received 11 Dec 2009; revised 7 Jan 2010; accepted 7 Jan 2010; published 12 Jan 2010

$$\varphi(t) = 2k\left[\left(z_0 - z_R\right) + v_z t + \left(\frac{\varepsilon''}{2k} + a_z\right)t^2\right]. \tag{5}$$

After the acquisition, the spectral interference signal is processed as shown in the diagram of Fig. 2. We start from the rescaled real spectra *S(k, t)* function of wavenumber *k* and transverse position *t.* A discrete Fourier transform is applied along the *k* direction to obtain an image whose dimensions are now the transverse position *t* and the depth *z* (Fig. 2(B)). This image has complex values, $\Gamma_{m,n}$, where *m* and *n* are indices corresponding to the transverse and depth positions, respectively. We can now write, for each pixel positioned at (*t, z*) with corresponding indices (*m, n*):

$$\Gamma_{m,n} = A_{m,n}\exp\left(i\,\varphi_{m,n}\right). \tag{6}$$

$\varphi_{m,n}$ is the phase term corresponding to Eq. (5).

The next step is the replacement of phase $\varphi_{m,n}$ of Eq. (6) by subtracting the phase of pixel (*m-1, n*) from that of pixel (*m, n*), that is $\varphi_{m,n} - \varphi_{m-1,n}$ (Fig. 2(C)). The new complex value of pixel (*m, n*) is then:

$$\tilde{\Gamma}_{m,n} = A_{m,n}\exp(i\,(\varphi_{m,n} - \varphi_{m-1,n}))\,. \tag{7}$$

Note here that the phase term of the first A-line (m = 0) of the B-scan is set to zero. Carrying out this phase subtraction is similar to differentiating the φ given by Eq. (5) with respect to *t*, yielding for the phase of Eq. (7):

$$\Delta\varphi = 2k\left[v_z + 2\Delta t\left(\frac{\varepsilon''}{2k} + a_z\right)\,t\right], \tag{8}$$

where Δt is the time interval between adjacent A-lines, equal to τ_A. We assume here constant v_z and a_z values between adjacent A-lines.

Then in the following step (Fig. 2(D)), as in the standard BM-scan method, a Fourier transform (along the *t* direction) is applied to this modified B-scan. From Eq. (8) we see that this results in a shift in the spatial frequency *f* domain of

$$2\tau_A\left(\varepsilon'' + 2ka_z\right). \tag{9}$$

The shift of Eq. (9) depends, on the EOM modulation ε'' and on the axial acceleration. Therefore, in contrast to the standard BM-scan method, it does not depend on the axial velocity. The complex conjugate is shifted in the opposite direction, namely, in the negative part of *f* domain. Again, the shift implied by EOM modulation is chosen to shift the real signal of a sample without acceleration at the center of the positive part of the *f* domain. If the sample is accelerating or has accelerating structures, an additional shift will be observed with respect to this EOM offset. The limit, $a_z^{\max}$, of the axial acceleration is given by $4ka_z^{\max}\tau_A^2 = \pi/4$ (where the band-pass filter bandwidth is set to be half of the positive *f* space or $\pi/2$) or $a_z^{\max} = \lambda/(32\tau_A^2)$. The $a_z^{\max}$ for our system (see Section 3), where λ_0 = 1020 nm and $1/\tau_A$ = 46.9 kHz is estimated to be $\cong$ 52,000 mm/s^2 (the medium refractive index is assumed to be 1.35). This acceleration value appears to be a safe upper value for retinal blood flow, even though it depends on the angle between the light beam and vessel direction. Finally an inverse Fourier transform along *f* is carried out and the full range image is obtained (Fig. 2(E)).

Consequently, the important point of this method is that it is not limited by the velocity of the sample and only a huge axial acceleration can corrupt the algorithm. This technique makes it possible: first, to keep the signal in the band-pass filter bandwidth (used to numerically clip

#121349 - $15.00 USD Received 11 Dec 2009; revised 7 Jan 2010; accepted 7 Jan 2010; published 12 Jan 2010

out the mirror image) and, second, to avoid possible shifts of the mirror signal of large velocity regions into the signal location in the *f* domain. With the proposed method, the shift from the EOM offset in the spatial frequency, *f*, is due to the axial acceleration and is thus expected to be smaller than that due to the axial velocity with the standard BM-scan method. Consequently, a smaller band-pass bandwidth can be chosen compared to that of the standard BM-scan method. This reduction makes it possible to increase the sensitivity since the noise is

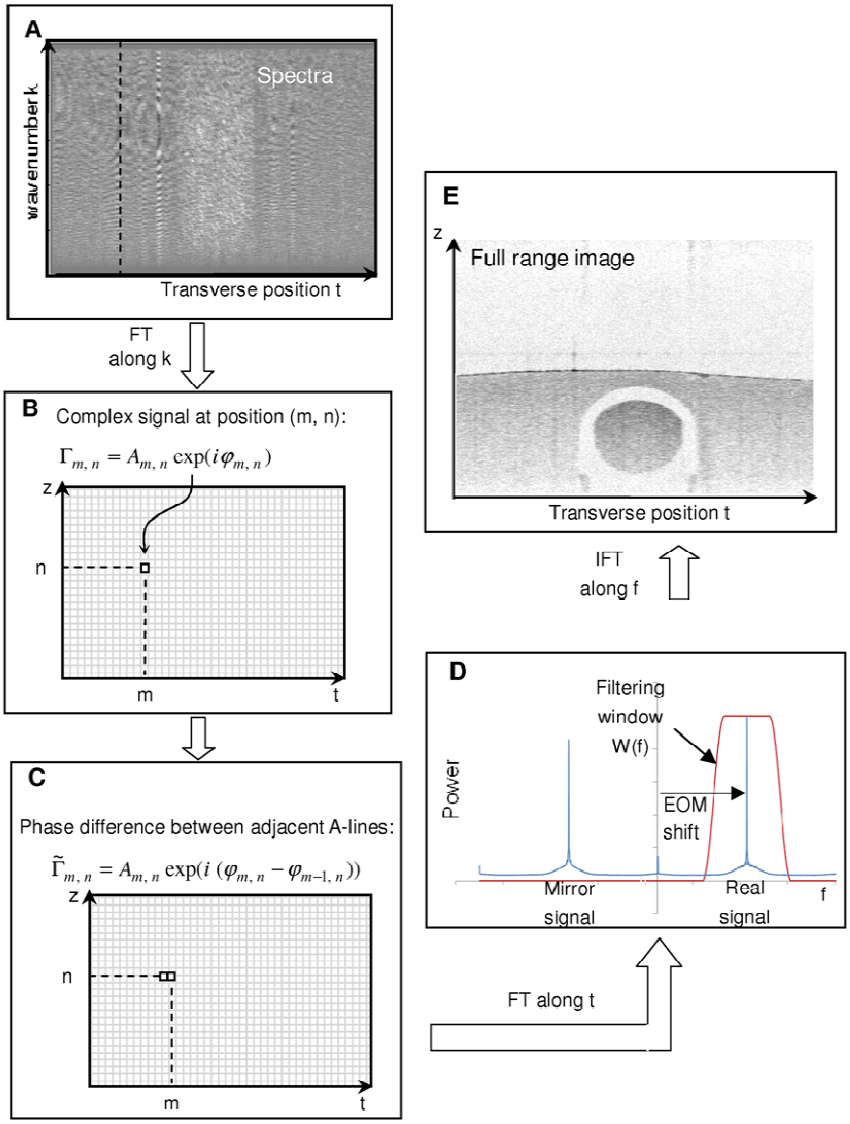

Fig 2. Diagram of the parabolic BM-scan technique: (A) Acquired rescaled real spectra displayed as a function of wavenumber *k* and transverse position *t*. Discrete Fourier transform (FT) along *k* is applied to obtain (B) the complex image function of depth *z* and transverse position *t*. A new image (C) is computed by replacing the phase term, $\varphi_{m,n}$, of pixel (*m, n*) of the image (B) by $\varphi_{m,n} - \varphi_{m-1,n}$. (D) A Fourier transform is carried out along the transverse direction, t, to remove the mirror signal in *f* space, as in the standard BM-scan method [27]. Finally the inverse Fourier transform (IFT) is computed to yield (E) the full range OCT image.

#121349 - $15.00 USD Received 11 Dec 2009; revised 7 Jan 2010; accepted 7 Jan 2010; published 12 Jan 2010

distributed over the *f* space. In the following experimental results, a flat-topped window *W(f)* is chosen for the band-pass filter [27]. Its bandwidth (at *W(f)* = 0) is equal to the width of the positive space of *f* for the standard BM-scan method (or $\pi/2$) and one half of the positive *f* domain for parabolic phase modulation (or $\pi/4$).

3. Experimental setup

A one-micrometer SD-OCT system was employed for the experimental verification of this new parabolic BM-scan method. The setup is depicted in Fig. 3. The broadband SLD light source (Superlum, Ireland) has a central wavelength of 1020 nm and a spectral width (FWHM) of 100 nm, resulting in a theoretical axial resolution of 3.4 μm in tissue. A 50/50 fiber splitter was used such that 50% of the light was delivered to the sample via a customized retinal scanner based on the 3D OCT-1000 (Topcon Corp., Tokyo, Japan). An EOM (EO-PM-NR-C2, Thorlabs, NJ) was positioned in the reference arm. A variable neutral density filter was placed in the reference arm in order to optimize the signal-to-noise ratio as close as possible to the shot-noise limit. The recombined light was collimated onto a brazed grating (1200 lp/mm, Thorlabs) and then passed through an achromatic lens pair (f = 200 mm and 150 mm, assembled into a composite lens with f = 88 mm).

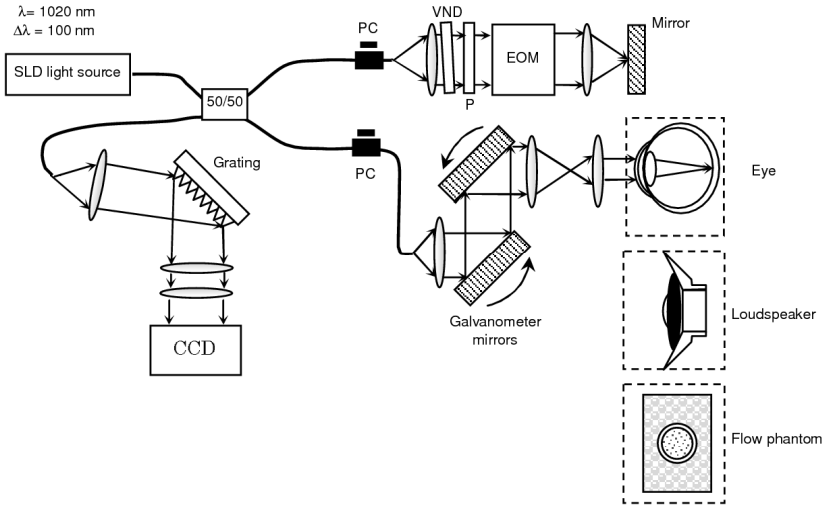

Fig. 3. Experimental SD-OCT set up. (PC): polarization controller, (VND): variable neutral density filter, (P): polarizer, (EOM): electro-optic modulator, (CCD): coupled charge device camera. Three samples are measured: a loudspeaker surface, a flow phantom and a human eye.

Finally, the resulting spectrum was acquired using a high-speed InGaAs scan camera (1024 pixels, 46.9 kHz line rate, SU1024LDH-1.7RT-0500LC, Sensors Unlimited Inc., Goodrich, NJ). The spectral interference signal was acquired through a Camera Link frame grabber board (PCIe-1429, National Instruments, TX). The data acquisition of the CCD camera, EOM phase modulation, and scanning of the probing arm were synchronized via control signals generated by a function generator board (PCI-6713, National Instruments) built into a standard PC.

#121349 - $15.00 USD Received 11 Dec 2009; revised 7 Jan 2010; accepted 7 Jan 2010; published 12 Jan 2010

4. Results

4.1 Quantitative comparison between standard and parabolic BM-scan methods

The difference between the performances of the linear and parabolic BM-scan methods was quantitatively examined. For this purpose, the surface of a vibrating loudspeaker was measured as a quantitative model of a moving sample.

In this experiment, transverse scanning was not performed. Hence, a B-scan image showed the time evolution of the A-line for a given location of the loudspeaker surface. Connected to a function generator, the vibration of the surface of the loudspeaker can be described by $z(t) = z_0 \sin(2\pi g t)$, where g is the frequency and z_0 is the amplitude of the vibration, which was calibrated by a standard SD-OCT measurement. Deriving $z(t)$ with respect to time t, the axial velocity for each A-line is written as: $v_z(t) = 2\pi g\ z_0 \cos(2\pi g t)$, varying between 0 and $2\pi g z_0$. The frequency was fixed at 100 Hz. The displacement amplitude was evaluated with the OCT image and was measured to be 31.5 μm from peak to peak. Therefore, the surface velocity varied between 0 and 9.9 mm/s. We imaged 3 cycles of the sine wave per B-scan, composed of 1,500 A-lines. Each A-line consisted of 1024 pixels. A single B-scan was acquired in 33.5 ms. Two B-scans were obtained, one with the linear BM-scan method and the other with the parabolic BM-scan method.

The OCT images are shown in Fig. 4(a) (linear BM-scan) and Fig. 4(b) (parabolic BM-scan). In both figures, the lower part corresponds to the real signal of the loudspeaker surface and the upper part to the mirror signal. The zero-delay line is the central horizontal line in the image (dash-dotted line). In Fig. 4(a), for the linear BM-scan, the mirror image is clearly seen (dark pixels), whereas for the parabolic BM-scan (Fig. 4(b)), the mirror image is strongly reduced. The broadening of the mirror image is due to the applied numerical dispersion compensation. In the case of the linear BM-scan method, the mirror image appears for large velocities of the loudspeaker surface. These high velocities are located between two successive peaks of the sinusoidal modulation. The maximal velocity of the loudspeaker, which is 9.9 mm/s in this particular experiment, is at the center point between successive peaks, and this maximal velocity exceeds the maximal allowable velocity of the method, 4.4 mm/s (Section 2.2). Hence, the linear BM-scan method is unable to remove the mirror image of these high velocity locations. The mirror image is only removed for the surface peaks (or low velocity). In contrast, the parabolic BM-scan method efficiently removes the mirror image for all velocities, where the maximal acceleration of the loudspeaker is 6,200 mm/s^2, and the maximal allowable acceleration is 52,000 mm/s^2 (Section 2.3).

#121349 - $15.00 USD Received 11 Dec 2009; revised 7 Jan 2010; accepted 7 Jan 2010; published 12 Jan 2010

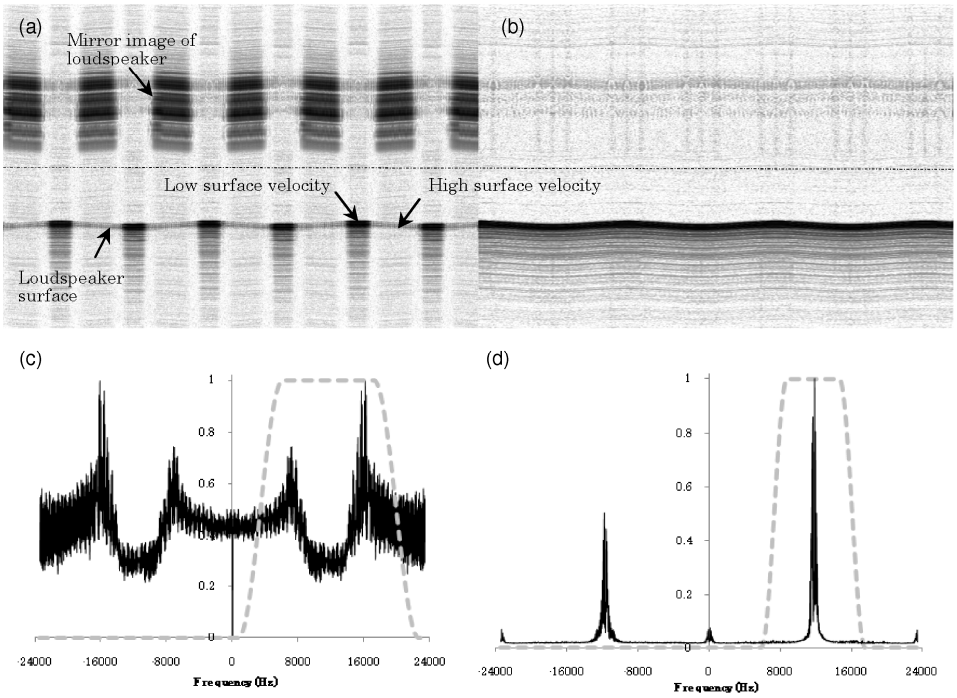

Fig. 4. OCT images for a given location of loudspeaker surface as a function of time for linear (a) and parabolic (b) phase modulation methods. The zero delay line is in the center of each image (dash-dotted line). Counter dispersion enlarges the spatial distribution of the imaginary image. (c) Normalized Spectrum as a function of temporal frequency obtained from (a). (d) Normalized Spectrum as a function of temporal frequency obtained from (b). Dashed curve is band pass filter. Spectra are obtained by taking the Fourier transform along horizontal lines, summed together and normalized by the maximum of this sum.

The failure of the linear BM-scan method can be understood as follows. As previously described (Section 2.1), the Fourier transform along the B-scan direction of each depth is carried out in the BM-scan technique. This gave us spectra as a function of the spatial frequency (*f* domain) for each depth. Examples of the normalized sum of the spectra over the depth are shown in Figs. 4(c) and 4(d), corresponding to the experiments of Figs. 4(a) (linear) and 4(b) (parabolic), respectively. The EOM modulation shifts the real signal to the center of positive *f* space, and the mirror signal to the center of negative *f* space. In the case of the linear BM-scan method (Fig. 4(c)), the spectrum was broadened due to the loudspeaker velocity. In other words, each A-line with a different velocity is shifted to a different position in this *f* space. The variation in the amount of shifting appears as a broadening of the signal in this sum of the spectra. The real signal and the mirror signal are overlapped. Consequently, the band-pass filter (the dashed line in Fig. 4(c)) is inefficient in mirror image elimination. On the other hand, in the case of the parabolic BM-scan method, the spectrum broadening is due to the acceleration of the loudspeaker surface. We see (Fig. 4(d)) that the spectrum broadening is small and the real signal remains located within the filter bandwidth (dashed line). Therefore, the mirror image is properly removed. Note in Fig. 4(d) that the mirror signal (left) and the real signal (right) are not symmetric to each other. This is due to the applied numerical dispersion compensation, which sharpens the real signal and blurs the mirror signal.

In order to quantify the efficiency of the mirror image removal, we computed the

#121349 - $15.00 USD Received 11 Dec 2009; revised 7 Jan 2010; accepted 7 Jan 2010; published 12 Jan 2010

extinction ratio (*ER*) of each A-line of the final OCT image of the surface of the loudspeaker. This extinction ratio is the ratio of the signal intensities of the real signal and its mirror signal.

We define the real surface signal as the average signal computed from the loudspeaker surface to 10 pixels below it. Since numerical dispersion compensation was utilized to visualize the real signal, we applied the corresponding opposite dispersion compensation to measure the mirror image signal at the mirror position of the loudspeaker surface. Hence, the dispersions of both the real signal and the mirror signal were correctly compensated.

Figure 5 shows the corresponding *ER* for both BM-scan methods: linear and parabolic. As mentioned above, the surface velocity varied between 0 and 9.9 mm/s. The loudspeaker surface displacement amplitude measured from the OCT image is also shown by a dashed curve. Comparing the surface displacement and *ER* as a function of time, we can evaluate the velocity range in which the linear BM-scan technique started to fail in removing the mirror image. For velocities ranging from 0 to 5.1 mm/s, the *ER* of the linear BM-scan method was approximately 20 dB. This ratio dropped to 10 dB for a velocity of 5.1 mm/s. Then, as the velocity, v, exceeded this value ($5.1 < v < 9.9$ mm/s), it reached a minimal value of approximately –27 dB. This negative value means that, due to the high velocity, the real signal was shifted out of the filter bandwidth in the spatial frequency domain, f, and replaced by the mirror signal. It is remarkable that the *ER* of the parabolic BM-scan method remained high and constant for all velocities, at a value of approximately 40 dB.

This simple experiment showed, in the case of a structure moving in the axial direction, that the robustness of the mirror image removal efficiency of the parabolic BM-scan method exceeds that of the linear BM-scan method.

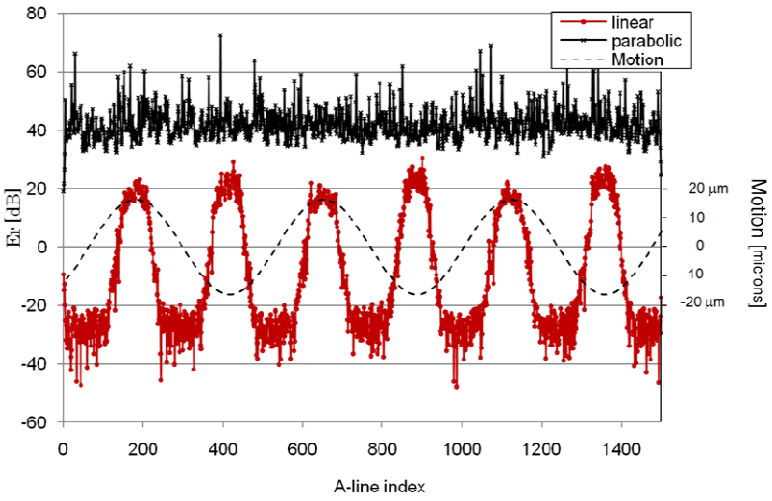

Fig. 5. Extinction ratios (*ER*) of the loudspeaker surface signal for linear and parabolic phase modulations as a function of time. Dashed curve represents the loudspeaker surface motion for the linear phase modulation.

4.2. In vivo comparison: retinal imaging

To visualize the mirror image artifact removal enhancement with the proposed technique for *in vivo* measurement, we imaged the retina of a human subject using both the standard and parabolic BM-scan methods.

The subject was a 33 year old male, and the incident power on the cornea was 1.3 mW,

#121349 - $15.00 USD Received 11 Dec 2009; revised 7 Jan 2010; accepted 7 Jan 2010; published 12 Jan 2010

which complied with the ANSI eye-safety standard [29]. The spot size on the retina was approximately 20 μm. A series of B-scans was acquired. In order to image the same region with both modalities, scanning was only performed in the x-direction ($\Delta y = 0$) and each B-scan was successively acquired with a different phase modulation; linear, parabolic, linear, and so on. The duration between each image acquired with a different phase modulation was 33.5 ms (1500 A-lines). Figures 6(a) and 6(b) show structural OCT images acquired with the linear and parabolic BM-scan methods, respectively. Figures 6(c) and 6(d) display the corresponding phase-resolved Doppler images obtained by the linear and parabolic BM-scan methods, respectively, where the solid arrows indicate the location of a large blood vessel.

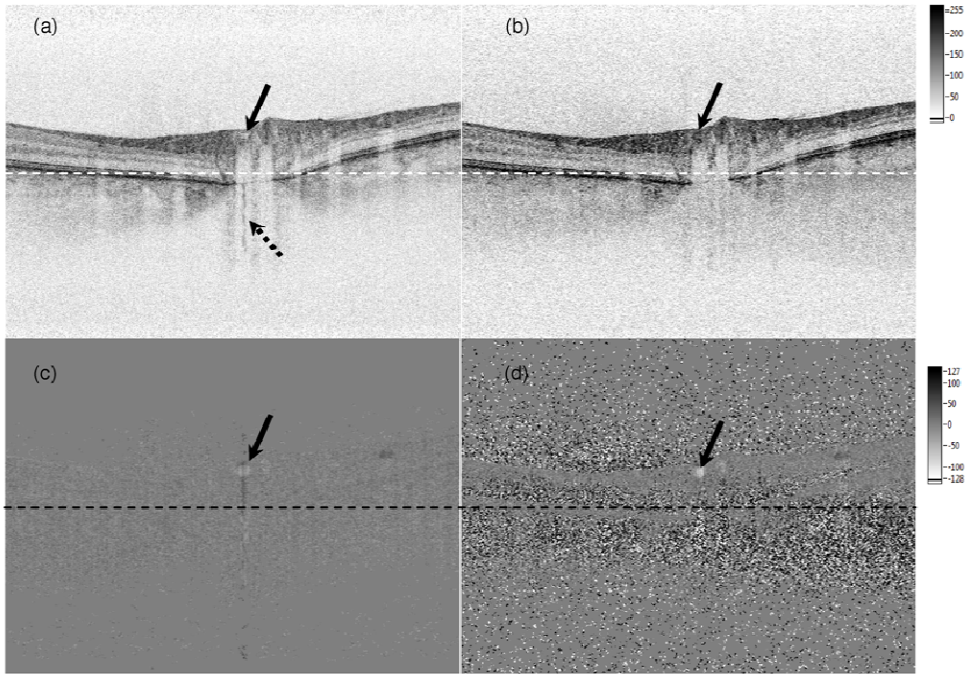

Fig. 6. Retina intensity OCT images for the linear (a) and parabolic (b) BM-scan techniques. Corresponding phase-resolved Doppler images for linear (c) and parabolic (d) methods. An inverted gray color map was used. The solid arrow indicates the vessel position and the dashed arrow its mirror image. The vessel's mirror image is not visible in the parabolic case. The dashed line is the zero delay line.

Figure 6(a) shows an OCT structural image acquired with the standard BM-scan method, with the mirror artifact caused by vessel flow visible as a wiggly vertical grey curve indicated by a dashed arrow. In the corresponding image acquired with the parabolic BM-scan method, shown in Fig. 6(b), this artifact is not perceptible. In the standard BM-scan Doppler image (Fig. 6(c)), we can see a vertical dark line at the vessel transverse position. This artifact exists because the vessel mirror image occupies a large part of the corresponding A-line. Consequently, the bulk motion compensation algorithm is unable to work properly. With the parabolic BM-scan method (Fig. 6(d)), no such artifact is seen. Note that the noise level is higher in the phase-resolved Doppler image of the parabolic BM-scan method. This is due to the phase differentiation carried out before the Fourier transform along the transverse direction (Section 2.3).

Therefore in the standard BM-scan method, mirror artifacts may be misinterpreted as

#121349 - $15.00 USD Received 11 Dec 2009; revised 7 Jan 2010; accepted 7 Jan 2010; published 12 Jan 2010

retinal structures. Moreover, with respect to Doppler phase-resolved images, the risk exists of velocity underestimation due to a mirror image artifact. This risk is reduced by the proposed technique. This issue is further examined and discussed in the following discussion section.

5. Discussion

Velocity retrieval may be hampered if the mirror image is not correctly removed. In this section, we quantitatively show the advantage of the parabolic BM-scan method compared to the standard BM-scan method. Phase-resolved Doppler measurements with a flow phantom were carried out for both methods.

A static sample was made by mixing gelatin with milk. A glass capillary (internal diameter: 780 microns, length: 10 cm) was embedded in this static sample and an intralipid solution (1%) flowed through it. The angle, θ, between the incident light beam and the capillary direction was obtained by acquiring the 3D OCT volume of the capillary. This angle was measured to be $\theta = 75$ degrees. The velocity of the solution was controlled by a syringe pump (Harvard Apparatus, MA). From the complex OCT image, we can compute the phase difference, $\Delta\varphi$, between adjacent A-lines, and obtain the corresponding phase-resolved Doppler image. First, for a given flow velocity (set by the pump), we select, in the phase-resolved Doppler image, the A-line passing by the center of the capillary. This corresponds to the maximum velocity, and consequently to the maximum phase shift. Then, the average is found by using its 10 adjacent A-lines (4 A-lines before and 5 A-lines after the maximum profile). The absolute velocity is then retrieved using the relationship between $\Delta\varphi$ and velocity v:

$$v = \frac{\lambda_0 \Delta\varphi}{4\pi n \tau_A \cos\theta}, \tag{10}$$

where λ_0 is the center wavelength of the light source in vacuum, and n is the refractive index of the medium (intralipid, $n = 1.35$). The axial velocity is given by: $v_z = v \cos\theta$ using v from Eq. (10). In the following, the term velocity refers to axial velocity.

The measured velocity as a function of the expected velocity (syringe pump settings) is plotted in Fig. 7. For the parabolic BM-scan method, the set velocity is retrieved ($R^2 = 0.98$) for the total range of set velocities (0 – 7 mm/s). However, for the standard BM-scan method, the linear relationship only held until the set velocity of 2.9 mm/s. Then, when the set velocity exceeds this critical velocity, the measured velocity drops to zero.

To theoretically determine the critical velocity, we have to consider the width of the band-pass filter applied to clip out the mirror image. This parameter determines the velocity limit of the standard BM-scan method, since the shift in f space is in proportion to the velocity. As can be seen in Fig. 4(c) (dashed curve), the band-pass filter employed was not a step function but a flat-topped window [27]. Consequently, if we consider the critical velocity that corresponds to the band-pass filter value of 0.5, we find a critical velocity of 3.1 mm/s (dashed line in Fig. 7). Beyond this limit, the velocity is underestimated since some portions of the signal are filtered out.

#121349 - $15.00 USD Received 11 Dec 2009; revised 7 Jan 2010; accepted 7 Jan 2010; published 12 Jan 2010

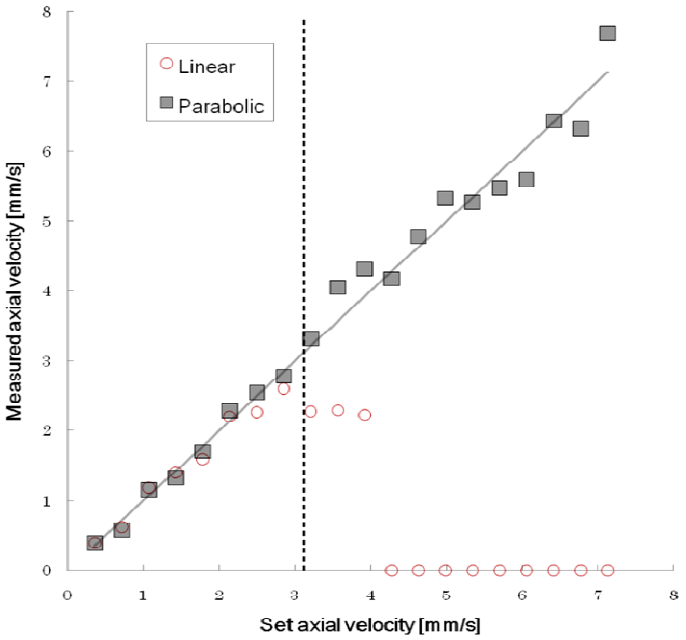

Fig. 7. Measured axial velocity as a function of the expected axial velocity (from the syringe pump settings) for the linear (standard BM-scan) and parabolic phase modulation techniques. The solid line has a slope = 1. The dashed line represents the axial velocity limit due to the band-pass filter bandwidth in the case of the linear phase modulation technique.

This signal loss is not due to phase wrapping, but is a limitation of the linear BM-scan method. Indeed, this loss is also visible in the structural OCT image. Figure 8 shows an example of the structural images obtained using both the standard and parabolic BM-scan methods at a given intralipid solution velocity of 6.1 mm/s. As can be seen in Fig. 8(a), in the case of the linear BM-scan method, the signal is missing at the center part of the capillary (solid arrow) where the velocity is maximal. The corresponding Doppler shift (16.1 kHz) exceeds half of the band width of the band-pass filter of the BM-scan analysis of 8.3 kHz. As discussed in Section 4.1, a signal with this critical Doppler frequency or higher moves to its mirror position, as indicated by the dashed arrow in Fig. 8(a). This signal loss is not seen in the parabolic BM-scan image (Fig. 8(b)). Again, the rationale is that, in the parabolic BM-scan method, the shift in the *f* domain is caused by the axial acceleration, which is small compared to the velocity. The parabolic BM-scan therefore extends velocity retrieval to larger axial velocities.

#121349 - $15.00 USD Received 11 Dec 2009; revised 7 Jan 2010; accepted 7 Jan 2010; published 12 Jan 2010

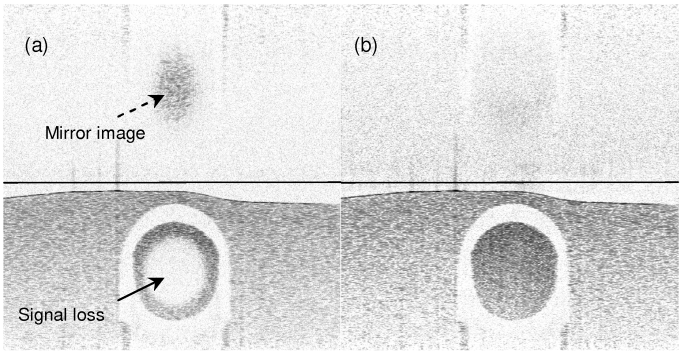

Fig. 8. OCT images acquired with (a) standard BM-scan technique and with (b) proposed technique. The flow phantom was made of a static sample (gelatin + milk) in which a glass capillary (inner diameter: 0.78 mm) was embedded. Intralipid (1%) solution flowed through it at a rate of 0.6 ml/min, with the maximal axial velocity v = 6.1 mm/s. The central line is the zero delay line.

6. Conclusion

We proposed a modified version of the BM-scan method that enables full range imaging of samples or inner structures with a large axial velocity. This was realized by two modifications of the standard BM-scan method. First, the EOM linear phase shift along the B-scan direction used in the standard BM-scan method was replaced by a parabolic phase shift. Second, the differentiation of the phase with respect to to transverse direction (B-scan direction) was performed before the Fourier transform in that direction. Consequently, the efficiency of the proposed method for mirror image elimination does not depend on the axial velocity but on the axial acceleration of moving structures. By using phantom experiments, we demonstrated that, in the case of moving structures with large velocities, the extinction ratio obtained with the parabolic BM-scan method was improved, which enabled better velocity estimation for large velocity structures. Moreover, we have shown, with *in vivo* imaging, that the proposed method allows mirror image removal of a retinal blood vessel, for which the standard BM-scan technique fails. Consequently, we believe that this mirror image removal technique may be helpful for ophthalmologic diagnoses where retinal blood flow measurements are required.

Acknowledgment

This study was partially supported by the Japan Society for the Promotion of Science (JSPS) through a Grant-in-aid for Scientific Research, 15760026, and by the Japan Science and Technology Agency through a contract of the development program for advanced measurement systems.

#121349 - $15.00 USD Received 11 Dec 2009; revised 7 Jan 2010; accepted 7 Jan 2010; published 12 Jan 2010